

Spontaneous Symmetry Breaking of an Optical Polarization State in a Polarization-Selective Nonlinear Resonator

K. S. Manannikov,* E. I. Mironova, and A. S. Poliakov

Department of Physics of Complex Systems, Weizmann Institute of Science, Israel

A. E. Ulanov

Deutsches Elektronen-Synchrotron DESY, Notkestr. 85, 22607 Hamburg, Germany

A. I. Lvovsky

Clarendon Laboratory, University of Oxford, Oxford OX1 3PU, UK

We exploit polarization self-rotation in atomic rubidium vapor to observe spontaneous symmetry breaking and bistability of polarization patterns. We pump the vapor cell with horizontally polarized light while the vertical polarization, which is initially in the vacuum state, is resonated in a ring cavity. Vacuum fluctuations in this mode experience cumulative gain due to the compound action of amplification due to the self-rotation and feedback through the resonator, eventually acquiring a macroscopic magnitude akin to an optical parametric oscillator. The randomness of these fluctuations results in a bistable, random macroscopic polarization pattern at the output. We propose utilizing this mechanism to simulate Ising-like interaction between multiple spatial modes and as a basis for a fully optical coherent Ising machine.

a. Introduction. A nonlinear optical effect known as polarization self-rotation (PSR) occurs as a result of interaction of elliptically polarized light with a non-linear $\chi^{(3)}$ medium. PSR consists in the rotation of the polarization ellipse at a rate that increases with the ellipticity [Fig. 1(a)]. The physics of PSR can be understood by considering the polarization pattern as a sum of two circular components of unequal intensities. In a Kerr medium, the refractive index for each component depends on its intensity. Unequal refractive indices result in different phase velocities, which, in turn, leads to the rotation of the polarization ellipse [Fig. 1(b)].

Initially investigated in the 1970's [1], PSR gained attention again in the early 2000's, when it was considered as a simple source of squeezed light [2], [3], [4]. If a PSR-exhibiting medium is pumped with linearly (e.g. horizontally) polarized light, vacuum fluctuations in the orthogonal (vertical) polarization mode can manifest as microscopic ellipticity of the overall polarization pattern. Microscopic self-rotation due to this ellipticity brings about linear shear of the phase space of the vertical polarization mode, squeezing the uncertainty circle.

In this work, we experimentally investigate optical parametric oscillation (OPO) induced by PSR. To that end, the effect on the vertical mode is enhanced by a cavity, in which that mode resonates [Fig. 1(c)]. For certain resonator lengths, the amplification becomes cumulative, leading to macroscopic electromagnetic field amplitude in the steady state and therefore macroscopic ellipticity of the field polarization in the vapor cell.

Our PSR-based OPO exhibits spontaneous symmetry breaking of the optical polarization state. The handedness of the steady-state elliptical pattern is determined

by the sign of the initial vacuum fluctuation from which it arose. As a result, this handedness is random every time the parametric oscillation is initiated and remains constant for as long as the oscillation is sustained. In other words, the polarization state is bistable.

Bistability is a common feature of parametric oscillators and Kerr cavities, observed in a variety of schemes [5]. For example, Moroney *et al.* [6] observed polarization bistability with a continuous wave in a high-Q fiber resonator with Kerr nonlinearity. Due to spontaneous symmetry breaking, one circular component of the linearly polarized input light became dominant inside the cavity, while the other one was reflected. However, due to residual cavity birefringence and imperfect input polarization, the transmitted polarization component was not completely random [6].

In our scheme, polarization selectivity of the resonator provides an additional degree of freedom and therefore much finer polarization control, leading to a random selection of one of the two helicities in the output. Moreover, atomic resonant enhancement leads to a much stronger nonlinearity than the $\chi^{(3)}$ nonlinearity in a fiber or the $\chi^{(2)}$ nonlinearity in a crystal: significant squeezing of a continuous wave mode can be obtained in a single pass through the vapor cell. This makes the scheme attractive for the implementation of all-optical coherent Ising machine. We discuss this idea at the end of the paper.

b. Concept. We analyze the transformation of the field polarization pattern under the joint action of PSR and the resonator. Interacting with a rubidium vapor cell, elliptically polarized light experiences rotation of its optical axis by the angle $\varphi(\varepsilon)$, where ε is the ellipticity. Subsequently, the vertical polarization is reflected by a polarizing beam splitter into the resonator. During a roundtrip through the resonator, the field accrues

* Corresponding author: konstantin.manannikov@weizmann.ac.il

a phase shift ψ and experiences a linear loss before being re-injected into rubidium. The field transformation in one roundtrip can thus be written as follows:

$$\begin{pmatrix} \mathcal{E}_H \\ \mathcal{E}_V^{(n+1)} \end{pmatrix} \quad (1) \\ = \begin{pmatrix} 0 & 0 \\ 0 & \sqrt{\eta}e^{i\psi} \end{pmatrix} \begin{pmatrix} \cos(\varphi) & -\sin(\varphi) \\ \sin(\varphi) & \cos(\varphi) \end{pmatrix} \begin{pmatrix} \mathcal{E}_H \\ \mathcal{E}_V^{(n)} \end{pmatrix} + \begin{pmatrix} \mathcal{E}_H \\ 0 \end{pmatrix},$$

where \mathcal{E}_H , \mathcal{E}_V are the complex field amplitudes of the polarization components in the n th roundtrip and $1 - \eta$ is the intensity loss in the cavity per roundtrip.

Figure 1(d) visualizes the evolution of \mathcal{E}_V in the complex plane. We use the horizontal component as phase reference, so \mathcal{E}_H is a real number. PSR admixes this real horizontal amplitude into the vertical mode [Fig. 1(d,ii)]. The subsequent roundtrip through the resonator rotates the complex phase of the field and scales it by factor $\sqrt{\eta}$ [Fig. 1(d,iii)]. The resulting vector undergoes further horizontal displacement due to self rotation (determined by the new ellipticity) [Fig. 1(d,iv)], and so on.

To identify the conditions under which this recurrent transformation leads to oscillation, we assume the initial ellipticity to be small ($\varepsilon \ll 1$). The self-rotation angle is then proportional to the ellipticity [2]:

$$\varphi \approx gl\varepsilon, \quad (2)$$

where the proportionality coefficient g depends on the intensity of the incident light and its detuning from resonance. The ellipticity itself (for $\mathcal{E}_H \in \mathbb{R}$) is defined as $\varepsilon = \arcsin \frac{\mathcal{E}_H \text{Im} \mathcal{E}_V}{|\mathcal{E}_H|^2 + |\mathcal{E}_V|^2}$ [2], simplifying to $\varepsilon \approx \frac{\text{Im} \mathcal{E}_V}{\mathcal{E}_H}$ for $\varepsilon \ll 1$. The vertical field component transformation according to Eq. (1) then becomes

$$\mathcal{E}_V^{(n+1)} \approx \sqrt{\eta}e^{i\psi}(\mathcal{E}_V + gl\text{Im}\mathcal{E}_V). \quad (3)$$

The threshold condition corresponds to $|\mathcal{E}_V^{(n+1)}| > |\mathcal{E}_V^{(n)}|$. This inequality can be solved by writing Eq. (3) in the matrix form with respect to the real and imaginary parts of \mathcal{E}_V and finding the eigenvalues $\lambda_{1,2}$ of the transition matrix. The threshold condition is obtained by requiring $\max_{\psi}(|\lambda_{1,2}|) > 1$, which resolves to

$$gl > 1/\sqrt{\eta} - \sqrt{\eta}, \quad (4)$$

with the highest gain observed at

$$\psi = \arctan\left(\frac{gl}{2}\right). \quad (5)$$

The infinite growth of $|\mathcal{E}_V|$ is limited by the pump depletion and saturation of the self-rotation coefficient for large ellipticities.

To obtain the polarization of the field in the steady state, the small-ellipticity condition must be relaxed, and Eq. (1) must be solved numerically.

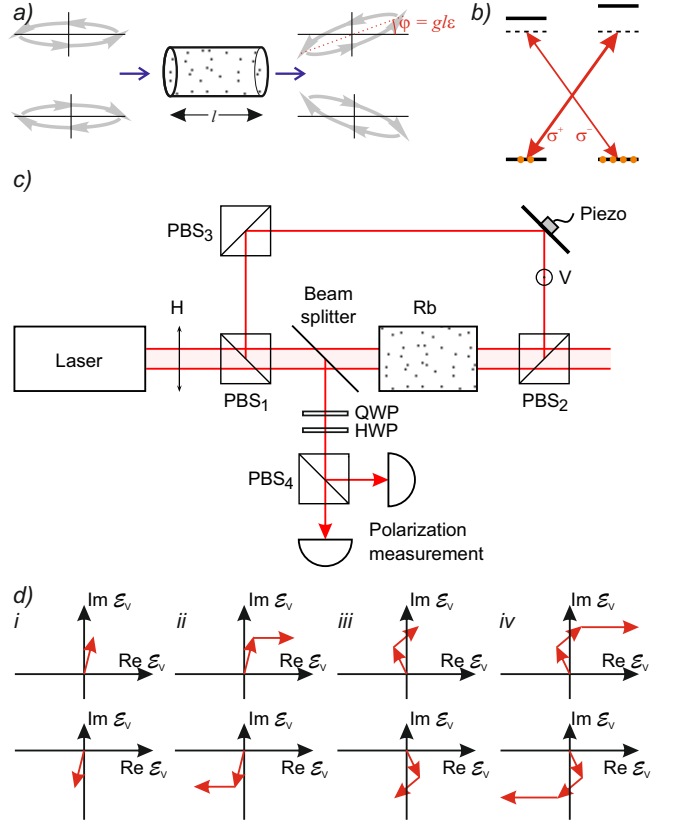


FIG. 1. Concept of the study. a) PSR effect. The magnitude and direction of self-rotation depend on the ellipticity of the input polarization and its handedness, respectively. b) Conceptual explanation of PSR in terms of atomic transitions. The two circular polarization components of the input field interact with the two legs of an X system. They experience different refractive indices unequal ground level population due to optical pumping and unequal AC Stark shifts. c) Scheme of the experiment. Rubidium vapor is pumped by horizontally polarized light, while the vertical polarization is resonated in a ring cavity. PBS: polarizing beam splitter; HWP: half-wave plate; QWP: quarter-wave plate. d) Origin of optical parametric oscillation and bistability. Complex electric field vector of the vertical polarization component is shown: (i) before entering the vapor cell, (ii) after passing through the cell and experiencing PSR, (iii) after a roundtrip through the cavity, before entering the cell for the second time, (iv) after second passage through the cell. The phase of the oscillation developed depends on the sign of the initial $\text{Im}\mathcal{E}_V$, giving rise to bistability (see text for further details).

The bistability of this PSR-based OPO can be understood by examining the top and bottom rows of Fig. 1(d). As is evident from Eq. (3), the sign of the imaginary component of \mathcal{E}_V (and hence the helicity of the polarization pattern) is preserved in each roundtrip through the resonator. Depending on the initial value of this sign, \mathcal{E}_V will amplify with one of the two opposite phases. Because the self-rotation angle $\varphi(\varepsilon)$ is an odd function of the ellipticity, it follows that whenever a vector $(\mathcal{E}_H, \mathcal{E}_V)$ with ellipticity ε is a steady state according to Eq. (1),

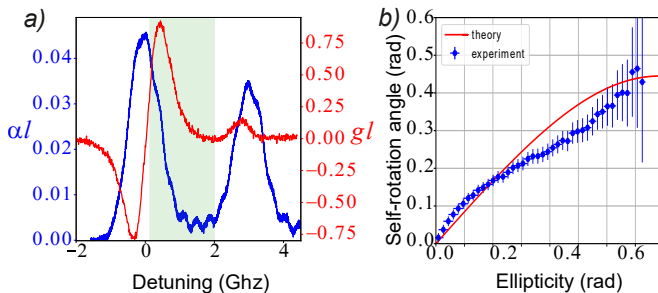


FIG. 2. Experimental observation of PSR. a) Coefficient of absorption αl (blue line, left scale) and self-rotation parameter gl (red line, right scale) measured across the ^{85}Rb D_1 transition. Zero detuning corresponds to the maximum absorption wavelength. The absorption coefficient αl is calculated as the natural logarithm of the ratio of the transmitted and input intensities. The green region marks the frequency range where bistability is observed. b) Dependence of the polarisation ellipse rotation angle on initial ellipticity at fixed pump power $P = 13.5$ mW and frequency detuning $\Delta = 0.35$ GHz. Experimental data (blue dots) is compared to the theoretically obtained curve (red line) from Eq. (6).

so is the vector $(\mathcal{E}_H, \mathcal{E}_V^*)$ with ellipticity $-\varepsilon$.

c. Experiment. We utilize a Vitawave external-cavity diode laser, which emits continuous-wave light at 795 nm with a power of 13.5 mW, resonant with the D_1 transition in ^{85}Rb . For PSR measurements, the laser polarization is set to horizontal polarization and directed into a rubidium cell heated to 70°C and placed inside a telescope formed by two $f = 30$ cm lenses. The transmitted beam is subjected to balanced polarimetric detection in a 45° basis (see Supplementary A for more experimental details).

The self-rotation is measured as a function of the laser detuning [Fig. 2(a)] and ellipticity [Fig. 2(b)]. For the latter dependence, we also obtain a theoretical prediction based on an X-shaped level structure [Fig. 1(b)] (Supplementary B):

$$\varphi = \frac{C\delta \sin(2\varepsilon)}{(2 + 8\delta^2) + [1 + \cos(4\varepsilon)]I/I_{\text{sat}}}, \quad (6)$$

where I is the optical intensity, I_{sat} the saturation intensity of the transition, δ the ratio of the detuning and the resonance line width, and C a proportionality coefficient. A good fit to the experimental data is found for $\delta = 0.1$ and $I/I_{\text{sat}} = 10$. We can see that the proportionality $\varphi \propto \varepsilon$ holds for small ellipticities.

To observe bistability, we construct the setup shown in Fig. 1(c) (see Supplementary D for details). The laser is tuned into the range with the lowest losses and the highest non-linearity [shown in pale green in Fig. 2(a)]. A small fraction of the field is deflected from the cavity before the cell with a high-transmissivity beam splitter, which was tested to have a negligible effect on the relative phase of the horizontal and vertical polarizations. The reflected beam is subjected to polarimetric measurement in the circular basis via two photodetectors.

The signal from these photodetectors, while the resonator phase is scanned with a piezoelectric transducer, is shown in Fig. 3(a). Whenever the phase passes through a cavity resonance, oscillation emerges with randomly either the right or left circular components being prevalent. The asymmetry between the two bistable states is due to experimental imperfections.

To investigate the dependence of the bistable state on the losses in the resonator, we measure the output polarization in circular and canonical bases to evaluate (see Supplementary C for a derivation):

$$\frac{\text{Im}\mathcal{E}_V}{\mathcal{E}_H} = \frac{I_L - I_R}{2I_H} \quad \text{and} \quad \frac{\text{Re}\mathcal{E}_V}{\mathcal{E}_H} = \frac{\sqrt{I_V - (\text{Im}\mathcal{E}_V)^2}}{\mathcal{E}_H}, \quad (7)$$

where I_R , I_L , and I_H are the intensities of the right circular, left circular, and horizontal polarization components respectively. The resulting data are demonstrated in Fig. 3(c). We observe that the bistability is significantly tolerant to losses, which is a consequence of a high phase-dependent gain in each roundtrip.

To demonstrate the randomness of the bistable states, we acquire a series of $M = 700$ oscillation events, ascribe a value $s_n = \pm 1$ to each event according to its helicity

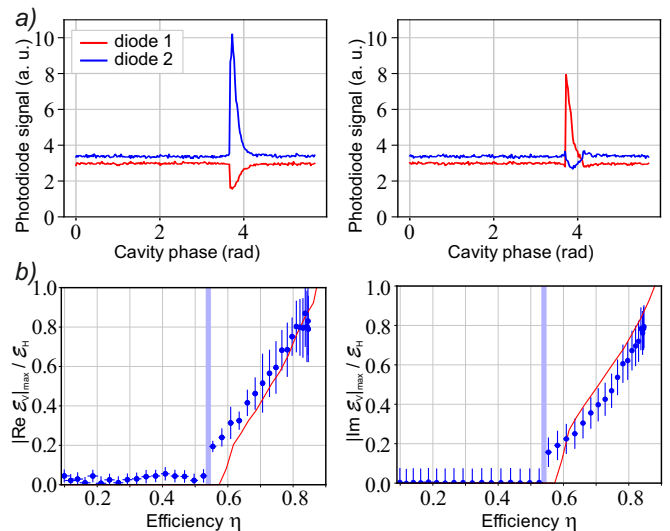


FIG. 3. Bistability measurements. a) Signals from the two photodiodes performing polarization measurements in the circular basis during two successive phase scans of the cavity. b) Real and imaginary parts of the steady-state vertical amplitude as a function of loss in the resonator. Vertical blue shaded area line is the threshold value calculated from Eq. (4). The red theoretical curve is obtained by numerically solving Eq. (1) with the self-rotation angle computed from Eq. (6). The blue shaded area shows the threshold calculated from Eq. (4) with the self-rotation parameter g obtained from the data in Fig. 2(b). All measurements are performed with a fixed frequency detuning $\Delta = 0.35$ GHz and pump power $P = 13.5$ mW.

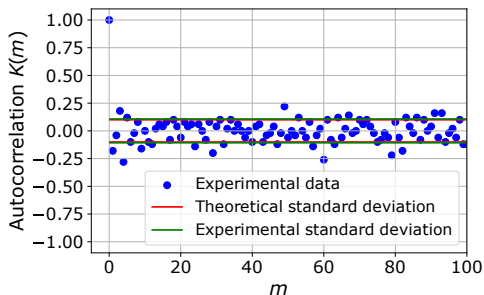


FIG. 4. Auto-correlation function for experimental values of binary phases (blue dots). Double standard deviation intervals for the experimental auto-correlation function and for the auto-correlation function of the ideal independent binary distribution are also shown.

and calculate the auto-correlation

$$K(m) = \frac{1}{M} \sum_{n=0}^{M-m} s_n \cdot s_{n+m}. \quad (8)$$

As can be seen in Fig. 4, this function behaves similarly to that of a fair coin: the standard deviations of $K(m)$ (for $m \neq 0$) for the experimental data and ideal Bernoulli distributions are almost equal. Such randomness can be a good basis for a random number generator [7, 8]. While the data in this experiment are acquired at a rate of 10–100 events per second, we expect the randomness to persist on time scales defined by atomic relaxation rates, i.e. tens of nanoseconds.

d. Summary and outlook. We demonstrated that polarization self-rotation could be utilized to generate bistable polarization states of light. Spontaneous symmetry breaking for the initial horizontally polarized light was achieved thanks to resonant optical nonlinearity of rubidium vapor cell in a vertical polarization selective resonator. As a result, the field in the resonator becomes elliptically polarized with a random helicity, as evidenced by statistical analysis.

The optical system presented in this paper can be scaled up: multiple independently bistable spatial modes

can be obtained simultaneously by focusing multiple spatially separated laser beams in the same vapor cell. These modes can be arbitrarily coupled by placing a spatial light modulator into the resonator. This system of coupled optical parametric oscillators would implement an all-optical coherent Ising machine (CIM), i.e. an analogue optical neural network capable of evolving into the ground state of an Ising Hamiltonian [9, 10].

In the original optoelectronic CIM [11–13], the pulsed modes are coupled through classical measurement and feedback, which precludes their entanglement and hence quantum computational advantage [14]. An all-optical CIM, in which the interaction between modes occurs via interference, would address this shortcoming. Existing solutions, based on pulsed modes and fiber interferometers, either involved very few oscillators [15] or had the coupling limited to nearest neighbours [16]. Leveraging the resolution of spatial light modulators to a couple of spatially separated continuous-wave bistable modes appears to be a promising path towards scalability.

In addition to applications for combinatorial optimization, it is interesting to explore the potential of this all-optical CIM as a quantum simulator of condensed matter physics. Such studies have been actively pursued with the D-Wave annealer, such as e.g. a recent simulation of nonequilibrium dynamics of a magnetic spin system undergoing a quantum phase transition [17]. The promise of multiple coupled OPOs in this context has been shown theoretically [18, 19], but there has been no reliable platform for experimental research.

The bistability, especially near the exceptional point, is highly sensitive to fluctuations of the system parameters, particularly an external magnetic field. Hence the setup may also prove promising as a magnetic field sensor.

To sum it up, the system studied here can be a basis for many academic and practical applications in quantum optics and analogue computing.

Acknowledgments. We are grateful to A. V. Masalov for support in the experiment and fruitful discussions. AL’s research is supported by the Innovate UK Smart Grant 10043476 and the NSERC Grant EP/Y020596/1.

-
- [1] P. Maker, R. Terhune, and C. Savage, Intensity-dependent changes in the refractive index of liquids, *Physical Review Letters* **12**, 507 (1964).
 - [2] A. Matsko, I. Novikova, G. R. Welch, D. Budker, D. Kimball, and S. Rochester, Vacuum squeezing in atomic media via self-rotation, *Physical Review A* **66**, 043815 (2002).
 - [3] J. Ries, B. Brezger, and A. Lvovsky, Experimental vacuum squeezing in rubidium vapor via self-rotation, *Physical Review A* **68**, 025801 (2003).
 - [4] E. E. Mikhailov and I. Novikova, Low-frequency vacuum squeezing via polarization self-rotation in rb vapor, *Optics letters* **33**, 1213 (2008).
 - [5] N. I. Zheludev, Polarization instability and multistability in nonlinear optics, *Soviet Physics Uspekhi* **32**, 357 (1989).
 - [6] N. Moroney, L. Del Bino, S. Zhang, M. Woodley, L. Hill, T. Wildi, V. J. Wittwer, T. Südmeyer, G.-L. Oppo, M. R. Vanner, *et al.*, A kerr polarization controller, *Nature communications* **13**, 398 (2022).
 - [7] T. Steinle, J. N. Greiner, J. Wrachtrup, H. Giessen, and I. Gerhardt, Unbiased all-optical random-number generator, *Physical Review X* **7**, 041050 (2017).
 - [8] L. Quinn, G. Xu, Y. Xu, Z. Li, J. Fatome, S. G. Murdoch, S. Coen, and M. Erkintalo, Random number generation using spontaneous symmetry breaking in a kerr resonator, *Optics Letters* **48**, 3741 (2023).

- [9] M. C. Strinati, I. Aharonovich, S. Ben-Ami, E. G. Dalla Torre, L. Bello, and A. Pe'er, Coherent dynamics in frustrated coupled parametric oscillators, *New Journal of Physics* **22**, 085005 (2020).
- [10] M. C. Strinati, L. Bello, E. G. Dalla Torre, and A. Pe'er, Can nonlinear parametric oscillators solve random ising models?, *Physical Review Letters* **126**, 143901 (2021).
- [11] T. Inagaki, Y. Haribara, K. Igarashi, T. Sonobe, S. Tamate, T. Honjo, A. Marandi, P. L. McMahon, T. Umeki, K. Enbutsu, *et al.*, A coherent ising machine for 2000-node optimization problems, *Science* **354**, 603 (2016).
- [12] P. L. McMahon, A. Marandi, Y. Haribara, R. Hamerly, C. Langrock, S. Tamate, T. Inagaki, H. Takesue, S. Utsunomiya, K. Aihara, *et al.*, A fully programmable 100-spin coherent Ising machine with all-to-all connections, *Science* **354**, 614 (2016).
- [13] T. Honjo, T. Sonobe, K. Inaba, T. Inagaki, T. Ikuta, Y. Yamada, T. Kazama, K. Enbutsu, T. Umeki, R. Kasahara, *et al.*, 100,000-spin coherent ising machine, *Science advances* **7**, eabh0952 (2021).
- [14] E. S. Tiunov, A. E. Ulanov, and A. Lvovsky, Annealing by simulating the coherent Ising machine, *Optics express* **27**, 10288 (2019).
- [15] A. Marandi, Z. Wang, K. Takata, R. L. Byer, and Y. Yamamoto, Network of time-multiplexed optical parametric oscillators as a coherent Ising machine, *Nature Photonics* **8**, 937 (2014).
- [16] T. Inagaki, K. Inaba, R. Hamerly, K. Inoue, Y. Yamamoto, and H. Takesue, Large-scale Ising spin network based on degenerate optical parametric oscillators, *Nat. Photon.* **10**, 415 (2016).
- [17] A. D. King, A. Nocera, M. M. Rams, J. Dziarmaga, R. Wiersema, W. Bernoudy, J. Raymond, N. Kaushal, N. Heinsdorf, R. Harris, *et al.*, Computational supremacy in quantum simulation, *arXiv preprint arXiv:2403.00910* (2024).
- [18] M. Calvanese Strinati, L. Bello, A. Pe'er, and E. G. Dalla Torre, Theory of coupled parametric oscillators beyond coupled ising spins, *Phys. Rev. A* **100**, 023835 (2019).
- [19] L. Bello, M. Calvanese Strinati, E. G. Dalla Torre, and A. Pe'er, Persistent coherent beating in coupled parametric oscillators, *Phys. Rev. Lett.* **123**, 083901 (2019).
- [20] J. Peatross and M. Ware, *Physics of light and optics* (Brigham Young University, Department of Physics Brigham, 2011).

SUPPLEMENTARY

A. Self rotation: experiment

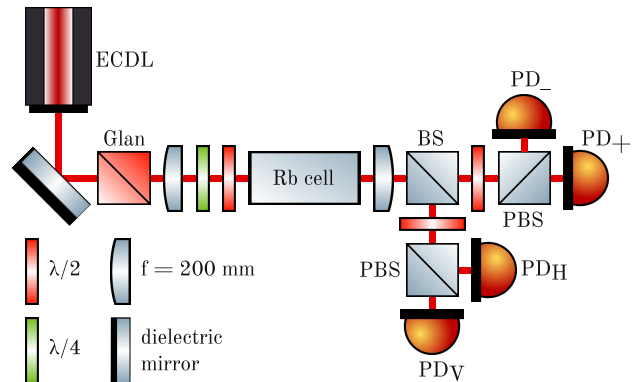


FIG. 5. Experimental setup for measuring PSR.

A scheme of the experimental setup for measuring PSR is shown in Fig. 5. The beam from an external cavity-diode laser (Vitawave ECDL-7950R) delivers approximately 50 mW of optical power in a single longitudinal mode. The laser is tuned across the rubidium D1 line ($\lambda \simeq 795$ nm). The beam is shaped by a pair of lenses and then transmitted through a Glan prism that transmits strictly linear polarization. A wave plate is placed before the Glan prism to vary the pump intensity; the transmitted intensity is 13.5 mW unless stated otherwise. The horizontally polarised light beam is then focused by a lens into a cylindrical vapour cell (25 mm in diameter and 75 mm in length) with antireflection coated windows, filled with ^{85}Rb without buffer gas at 70°C . With an estimated focal beam diameter of $d = 50 \mu\text{m}$, we experimentally obtain $I_{\text{sat}} \simeq 0.8 \text{ mW}/\pi d^2$, thus operating in a high saturation regime.

To produce and control ellipticity in the initially horizontally polarised beam, a fine-adjustable $\lambda/4$ plate is placed in front of the cell. To compensate for the impact of birefringent windows on pumping light, we align the major axis of the polarisation ellipse with the optical axis of the cell windows. To this end, we place a $\lambda/2$ wave plate after the $\lambda/4$ plate and adjust it every time we rotate the latter to and check that the polarization pattern does not rotate when the laser is tuned into and out of the atomic line.

After exiting the cell, the beam is directed to the measuring system consisting of a $\lambda/2$ wave plate and a PBS, whose axis is aligned with the Glan prism. By rotating this $\lambda/2$ plate, we can measure the signal in either canonical or diagonal basis. The outputs of the PBS are directed to two photodiodes. Data are gathered by tuning the laser through the rubidium D1 line for a range of initial ellipticities and recording the signal from the photodiodes. The rotation angle of the polarisation ellipse is

determined by (see Supplementary C)

$$\varphi = \frac{1}{2} \arctan \left(\frac{I_+ - I_-}{I_+ + I_- - 2I_V} \right), \quad (9)$$

where I_{\pm} and I_V are the intensities of the $\pm 45^\circ$ and vertical polarizations, respectively. The measurements were performed with a small initial ellipticity ε and the input intensity significantly below saturation. The data obtained under these conditions are shown in Fig. 2 of the main text and supplemented here in Figs. 6

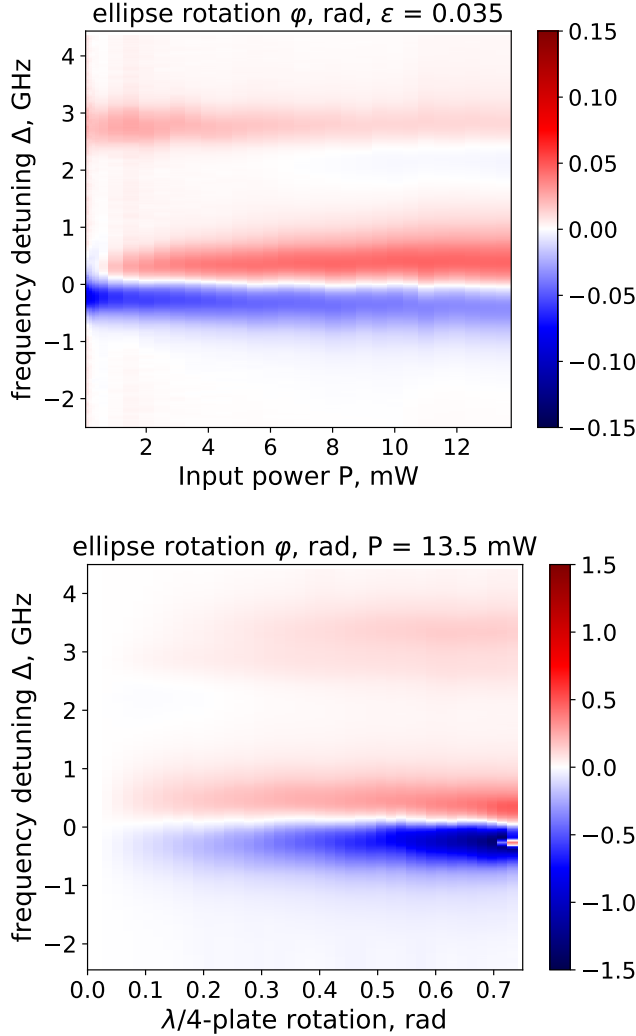


FIG. 6. Spectrum of the PSR angle φ . (a) Ellipticity $\varepsilon = 0.035$ fixed, optical power variable. (b) Optical power $P = 13.5$ mW fixed, ellipticity variable.

B. Self-rotation in an atomic X system

We develop the theory of PSR and Eq. (6) assuming X-shaped level structure as shown in Fig. 7. The Hamiltonian of this system under the rotating-wave approxi-

mation is as follows:

$$\hat{H} = \hbar \begin{pmatrix} 0 & -\Omega_R & 0 & 0 \\ -\Omega_R^* & -\Delta & 0 & 0 \\ 0 & 0 & 0 & -\Omega_L \\ 0 & 0 & -\Omega_L^* & -\Delta \end{pmatrix}, \quad (10)$$

We solve the master equations

$$\begin{aligned} \dot{\rho}_{11} &= \Gamma \rho_{44} + \gamma \rho_{22} + i\Omega_R \rho_{12}^* - i\Omega_R^* \rho_{12} \stackrel{!}{=} 0; \\ \dot{\rho}_{22} &= -\Gamma \rho_{22} - \gamma \rho_{22} - i\Omega_R \rho_{12}^* + i\Omega_R^* \rho_{12} \stackrel{!}{=} 0; \\ \dot{\rho}_{33} &= \Gamma \rho_{22} + \gamma \rho_{44} + i\Omega_L \rho_{34}^* - i\Omega_L^* \rho_{34} \stackrel{!}{=} 0; \\ \dot{\rho}_{44} &= -\Gamma \rho_{44} - \gamma \rho_{44} - i\Omega_L \rho_{34}^* + i\Omega_L^* \rho_{34} \stackrel{!}{=} 0; \\ \dot{\rho}_{12} &= -\left(\frac{\gamma + \Gamma}{2} + i\Delta\right) \rho_{12} - i\Omega_R (\rho_{11} - \rho_{22}) \stackrel{!}{=} 0; \\ \dot{\rho}_{34} &= -\left(\frac{\gamma + \Gamma}{2} + i\Delta\right) \rho_{34} - i\Omega_L (\rho_{33} - \rho_{44}) \stackrel{!}{=} 0; \\ \dot{\rho}_{24} &= -\Omega_R^* \rho_{14} - \Omega_L \rho_{23} \stackrel{!}{=} 0; \\ \dot{\rho}_{23} &= i\Delta \rho_{23} + \Omega_R^* \rho_{13} - \Omega_L^* \rho_{24} \stackrel{!}{=} 0; \\ \dot{\rho}_{14} &= -i\Delta \rho_{14} + \Omega_R \rho_{24} - \Omega_L \rho_{13} \stackrel{!}{=} 0; \\ \dot{\rho}_{13} &= -\Omega_R \rho_{23} - \Omega_L^* \rho_{14} \stackrel{!}{=} 0 \end{aligned}$$

for a steady state under the condition $\text{Tr}(\rho_{11} + \rho_{22} + \rho_{33} + \rho_{44}) = 1$ with $\Omega_{R,L} = \frac{d_{R,L} \mathcal{E}_{R,L}}{\hbar}$. We look for the susceptibilities $\chi_{R,L} = N \text{Tr} \hat{\rho} \hat{d}_{R,L}$ for the right and left circular polarizations, which are proportional to the mean values of the dipole moment operators

$$\hat{d}_R = \begin{pmatrix} 0 & d & 0 & 0 \\ d & 0 & 0 & 0 \\ 0 & 0 & 0 & 0 \\ 0 & 0 & 0 & 0 \end{pmatrix}; \quad \hat{d}_L = \begin{pmatrix} 0 & 0 & 0 & 0 \\ 0 & 0 & 0 & 0 \\ 0 & 0 & 0 & d \\ 0 & 0 & d & 0 \end{pmatrix}, \quad (11)$$

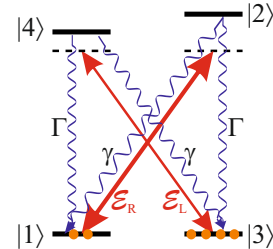


FIG. 7. Schematic diagram of energy levels with possible transitions.

yielding the refractive indices for the two polarizations:

$$n_R - 1 \approx \frac{1}{2}\chi_R = N \frac{\text{Re}(d_R \rho_{12})}{\mathcal{E}_R} \quad (12)$$

$$\sim N \frac{\delta}{(1 + 4\delta^2) \frac{I_R}{I_L} + \left(1 + 4\delta^2 + 4 \frac{I_R}{I_{\text{sat}}}\right)}$$

$$n_L - 1 \approx \frac{1}{2}\chi_L = N \frac{\text{Re}(d_L \rho_{34})}{E_L} \quad (13)$$

$$\sim N \frac{\delta}{(1 + 4\delta^2) + \left(1 + 4\delta^2 + 4 \frac{I_R}{I_{\text{sat}}}\right) \frac{I_L}{I_R}},$$

where N is the number density, $\delta = \frac{\Delta}{\Gamma + \gamma}$ and $I_{\text{sat}} = \frac{c\epsilon_0 \hbar^2 (\Gamma + \gamma)^2}{4\pi d^2}$. This gives the self-rotation angle

$$\varphi(\varepsilon) = -\frac{1}{2}kl(n_R - n_L) \quad (14)$$

$$\sim \frac{\delta \sin(2\varepsilon)}{(2 + 8\delta^2) + I/I_{\text{sat}} + \cos(4\varepsilon)I/I_{\text{sat}}}$$

C. Deriving Eqs.(7) and (9)

Let us define $\mathcal{E}_V \equiv V e^{i\beta}$, $\mathcal{E}_H \equiv H$ (we recall that the phase reference is such that $\mathcal{E}_H \in \mathbb{R}$). The polarization state $\begin{pmatrix} \mathcal{E}_H \\ \mathcal{E}_V \end{pmatrix}$ can be decomposed in the diagonal basis:

$$\begin{pmatrix} H \\ V e^{i\beta} \end{pmatrix} = \frac{\mathcal{E}_+}{\sqrt{2}} \begin{pmatrix} 1 \\ 1 \end{pmatrix} + \frac{\mathcal{E}_-}{\sqrt{2}} \begin{pmatrix} 1 \\ -1 \end{pmatrix}, \quad (15)$$

from which we find $I_{\pm} \equiv |\mathcal{E}_{\pm}|^2 = \frac{1}{2}((H \pm V \cos \beta)^2 + V^2 \sin^2 \beta)$, and therefore

$$\cos \beta = \frac{|\mathcal{E}_+|^2 - |\mathcal{E}_-|^2}{2HV}. \quad (16)$$

The angle φ between the major axis of the polarization ellipse $(\mathcal{E}_H, \mathcal{E}_V)$ and horizontal is given by [20]

$$\varphi = \frac{1}{2} \arctan\left(\frac{2HV \cos \beta}{H^2 - V^2}\right)$$

$$= \frac{1}{2} \arctan\left(\frac{|\mathcal{E}_+|^2 - |\mathcal{E}_-|^2}{|\mathcal{E}_+|^2 + |\mathcal{E}_-|^2 - 2V^2}\right)$$

$$= \frac{1}{2} \arctan\left(\frac{I_+ - I_-}{I_+ + I_- - 2I_V}\right),$$

where we used Eq. (16) and that $|H|^2 + |V|^2 = |\mathcal{E}_+|^2 + |\mathcal{E}_-|^2$.

To derive Eq. (7), we use the circular basis:

$$\begin{pmatrix} \mathcal{E}_H \\ \mathcal{E}_V \end{pmatrix} = \begin{pmatrix} \mathcal{E}_H \\ \text{Re}\mathcal{E}_V + i\text{Im}\mathcal{E}_V \end{pmatrix} = \frac{\mathcal{E}_R}{\sqrt{2}} \begin{pmatrix} 1 \\ i \end{pmatrix} + \frac{\mathcal{E}_L}{\sqrt{2}} \begin{pmatrix} 1 \\ -i \end{pmatrix}, \quad (17)$$

which gives $I_R = |\mathcal{E}_R|^2 = \frac{1}{2}((\mathcal{E}_H - \text{Im}\mathcal{E}_V)^2 + (\text{Re}\mathcal{E}_V)^2)$, $I_L = |\mathcal{E}_L|^2 = \frac{1}{2}((\mathcal{E}_H + \text{Im}\mathcal{E}_V)^2 + (\text{Re}\mathcal{E}_V)^2)$. Hence

$$\frac{\text{Im}\mathcal{E}_V}{\mathcal{E}_H} = \frac{I_L - I_R}{2I_H},$$

$$\frac{\text{Re}\mathcal{E}_V}{\mathcal{E}_H} = \frac{\sqrt{I_V - (\text{Im}\mathcal{E}_V)^2}}{\mathcal{E}_H} = \frac{\sqrt{4I_V I_H - (I_L - I_R)^2}}{2I_H}. \quad (18)$$

D. Full experimental setup

We use an additional rubidium cell as a reference to determine the laser frequency using absorption spectroscopy. Waveplates before and after the rubidium cell are needed to compensate the birefringence of the cell's windows. Resonator losses are controlled by rotating the $\lambda/2$ plate in front of PBS₃ in the resonator loop (Fig. 8).

To compensate for the birefringence of the cell windows and other imperfections of the setup, the polarization of the input beam is fine-tuned by two waveplates before the cell to eliminate the cavity resonance peaks when the laser is detuned from the atomic line. The cavity is aligned to maximize the mode matching between the horizontally polarized light returning from PBS₃ and the horizontal pump by observing interference between the two fields. We achieve the maximum visibility of $V = 0.96 \pm 0.01$, which corresponds to a mode-matching efficiency of $V^2 \approx 0.92$.

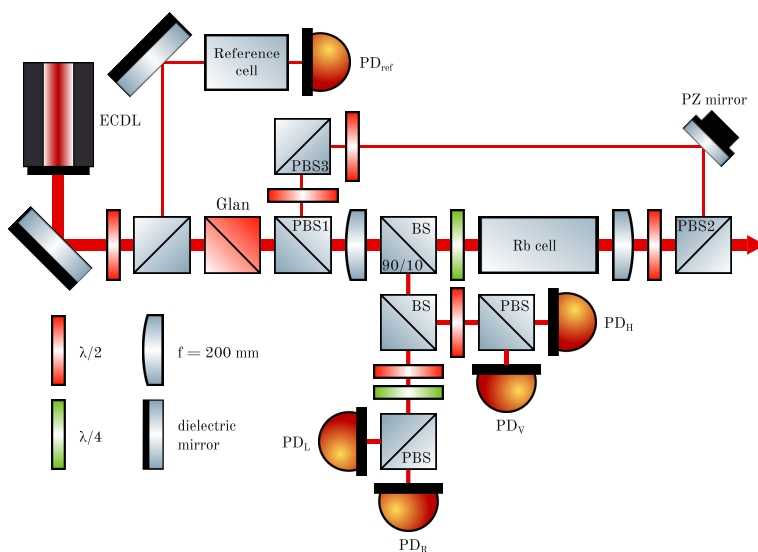


FIG. 8. Full experimental setup.